Annals of Glaciology

Article

Cite this article: Simenhois R, Birkeland KW, Gaume J, van Herwijnen A, Bergfeld B, Trottet B, Greene E (2023). Using video detection of snow surface movements to estimate weak layer crack propagation speeds. *Annals of Glaciology* 1–11. https://doi.org/10.1017/aog.2023.36

Received: 29 December 2022
Revised: 10 April 2023
Accepted: 15 April 2023

Keywords:
Avalanches; snow

Corresponding author:
Ron Simenhois;
Email: ron.simenhois@state.co.us

cambridge.org/aog

Using video detection of snow surface movements to estimate weak layer crack propagation speeds

Ron Simenhois[1], Karl W. Birkeland[2], Johan Gaume[3,4,5], Alec van Herwijnen[4], Bastian Bergfeld[4], Bertil Trottet[6] and Ethan Greene[1]

[1]Colorado Avalanche Information Center, Boulder, CO, USA; [2]USDA Forest Service National Avalanche Center, Bozeman, MT, USA; [3]Institute for Geotechnical Engineering, ETH Zurich, Zurich, Switzerland; [4]WSL Institute for Snow and Avalanche Research SLF, Davos Dorf, Switzerland; [5]Climate Change, Extremes, and Natural Hazards in Alpine Regions Research Center CERC, Davos Dorf, Switzerland and [6]School of Architecture, Civil and Environmental Engineering, Swiss Federal Institute of Technology, Lausanne, Switzerland

Abstract

Dry-snow slab avalanches release due to crack propagation in a weak snow layer under a cohesive snow slab. Crack propagation speeds can provide insights into the potential size of avalanches and inform fracture and avalanche release models. Despite their importance, slope-scale crack speed measurements from real avalanches are limited. Further, most existing slope-scale measurements utilize the appearance of slab fractures on the snow surface. However, we have no evidence that the appearance of surface cracking is a good indicator of the weak layer crack propagation tip. Here we present a novel method to estimate crack propagation speed from snow surface movements in avalanche videos. Our technique uses changes in frame pixel intensity, allowing us to detect the location of weak layer cracks well before slab fractures appear on the snow surface. We use field experiments and numerical simulations to validate our method before applying it to five avalanches. Our estimates show that cracks propagate faster up and down the slope than in the cross-slope direction; this suggests that different propagation regimes likely govern crack propagation up/down the slope, cross-slope and in flat terrain.

Introduction

Dry-snow slab avalanches result from a sequence of fracture processes. First, weak layer failure initiates under a cohesive slab, resulting in a localized crack. Second, once that crack expands to a critical size, r_c, crack propagation begins. Third, the crack extends across the slope, a process called dynamic crack propagation. Finally, avalanche release occurs if the tangential component of the gravitational load due to the slab overcomes frictional resistance to sliding. Eventually, cracks initiate at the avalanche's crown, flanks and stauchwall (Schweizer and others, 2003; Schweizer and others, 2016).

Spatial variations in slab and weak layer properties may arrest fracture during the dynamic crack propagation phase. For example, fracture may arrest in localized areas with stronger weak layers because the energy required to extend the crack may exceed the energy released during crack extension (Jamieson and Johnston, 1992; Gaume and others, 2015). If such local variations are small enough, the kinetic energy of the propagating crack may overcome this energy deficit, thereby maintaining crack propagation (Broberg, 1996). Indeed, video analyses of Propagation Saw Tests (PSTs) (Gauthier and Jamieson, 2006) shows that faster propagating cracks tend to propagate longer distances (van Herwijnen and others, 2016). However, the underlying reason for the correlation between crack speed and propagation distance is not yet fully understood. Another factor correlated with crack speed is slab density, with higher densities supporting faster propagation (Heierli, 2005; McClung, 2005; Bergfeld and others, 2022, 2023). The stronger slabs associated with these high densities allow for greater crack propagation distances, which may release larger avalanches (Gaume and others, 2015).

Despite the significance of crack speed (Gross and Seelig, 2017), relatively few direct measurements exist over distances exceeding a few meters or in actual avalanche start zones. Johnson and others (2004) made one of the first direct measurements of crack speed, using geophones in flat terrain to measure a crack speed of $20 \pm 2\,\mathrm{m\,s^{-/}}$ over 8 meters. van Herwijnen and Jamieson (2005) reported similar speeds on isolated beams, with values ranging between 17 and 26 $\mathrm{m\,s^{-1}}$. Crack propagation speed measurements made with high-speed videos of PSTs combined with particle tracking velocimetry (PTV) range from 10 to 50 $\mathrm{m\,s^{-1}}$ (van Herwijnen and Jamieson, 2005; Bair and others, 2014; van Herwijnen and Birkeland, 2014; van Herwijnen and others, 2016). van Herwijnen and Schweizer (2011) used a seismic sensor array to estimate a crack speed of $42 \pm 4\,\mathrm{m\,s^{-1}}$ for an avalanche that was 60 m wide in Switzerland, and van Herwijnen (2005) analyzed 11 avalanche videos to calculate speeds ranging from 15 to 32 $\mathrm{m\,s^{-1}}$. Similar speed values were also reported based on numerical simulations of the PST (Gaume and others, 2015). More recently, Bergfeld and others (2022, 2023) used synchronized accelerometers to measure a crack propagation speed of $49 \pm 5\,\mathrm{m\,s^{-1}}$ over 25 m of flat terrain. Bergfeld and others (2021) and Bergfeld and others (2018) used Digital Image

Correlation (DIC) to measure crack speeds between 20 and 30 m s^{-1} and between 37 and 45 m s^{-1}, respectively, in a 3.3 m PSTs. Bergfeld and others (2018, 2022, 2023) used DIC again to measure crack propagation speeds on long PST experiments (up to 9 m long) over the entire life cycle of a weak layer. They measured speeds as fast as 55 ± 8 m s^{-1}. Hamre and others (2014) analyzed videos of avalanches to estimate crack speeds that were much faster. Some of their crack speeds approached 200 m s^{-1}, with an average speed of 80 m s^{-1} for 27 videos.

Crack speed estimates from PSTs, collapsing weak layers on flat terrain, and cross-slope propagation in avalanches and numerical models are limited by the flexural wave speed of the slab (Bergfeld and others, 2021) and align with theoretical predictions of incipient shear cracks of 29–41 m s^{-1} (McClung, 2005) and asymptotic flexural speeds of 2126 m s^{-1} (Heierli and others, 2008). However, the much higher speeds in some avalanches estimated by Hamre and others (2014) contradict those theoretical predictions. Recent modeling by Gaume and others (2018, 2019), Trottet and others (2022) and Bobillier and others (2023) suggested that the processes governing crack propagation vary between flat terrain and in different directions on slopes. Their speed estimates on low-angle terrain align with those from theoretical models and experimental measurements. However, on slopes steeper than the snow friction angle they report a transition from relatively slower anticrack propagation to much faster supershear crack propagation with intersonic crack speeds. Thus far, few crack speed measurements on real slope-scale avalanches exist to verify these model predictions. There have been many measurements of weak layer crack speeds, but most are on low-angle terrain or at scales smaller than a typical avalanche starting zone (<5 m).

Except for the avalanche measured by van Herwijnen and Schweizer (2011), all experimental crack speeds measured at a larger scale on steep slopes are indirect crack speed measurements relying on video frame measurements of visible surface cracks (van Herwijnen and Jamieson, 2005; Hamre and others, 2014; Bergfeld and others, 2021). Bergfeld and others (2021) suggest the error associated with this method becomes negligible for large avalanches (⩽5% crack propagation speed for crack propagation over 200 m). However, this technique is limited because videos of such large crack propagations are rare and are typically in the cross-slope direction. To estimate crack speeds at the scale of small and medium-size avalanches, we present a novel method that allows us to track snow surface movements resulting from weak layer crack propagation before visible cracks appear on the snow surface (Fig. 1). We use this method to estimate crack propagation speed in both slope-parallel and cross-slope directions, and we track snow surface movements from the onset of weak layer crack propagation to the beginning of downslope slab movement.

Methods

Assumptions

Our approach assumes that only minor changes in pixel intensity occur due to factors that change slowly relative to the length of our measurement time window, such as cloud cover or the sun's angle. The time between crack initiation and the emergence of cracks on the snow surface is on the order of 1 s. We employed a masking technique to exclude areas of the slope where rapid fluctuations in pixel intensities were caused by movements, such as human activity, shadows or rolling snowballs, to ensure these areas were not mistakenly detected as slab crack propagation-driven movements.

Video processing

Our technique for estimating crack speeds from videos assumes that the most significant changes in pixel intensity are due to snow surface movement associated with weak layer fracture (Fig. 2). Our method requires three steps: (1) video stabilization, (2) tracking snow surface movement by detecting small changes in snow reflection and (3) estimating crack speed by using motion segmentation to highlight changes between consecutive video frames (Fig. 1).

In the first step, we converted the video to grayscale and used an optical flow algorithm introduced by Lucas and Kanade (Lucas and others, 1981) to stabilize our videos. We calculated the linear transformation matrix M between two consecutive video frames from motion vectors of pixels around static terrain features like rocks and snow roughness. We manually selected an area in the video with static terrain features and used the Shi-Tomasi Good Feature to Track algorithm (Shi and others, 1994) to select the feature for the optical flow.

The Lucas–Kanade method assumes that the displacement of the image contents between two consecutive video frames is small and approximately constant within neighboring pixels of a point p.

We then assume that the optical flow equation holds for all pixels within a window centered at p.

Namely, the local velocity vector (V_x, V_y) must satisfy the following:

$$I_x(q_j)V_x + I_y(q_j)V_y = I_t(q_j) \tag{1}$$

where q_j are the individual pixels inside the window centered around point p, and $I_x(q_j)$, $I_y(q_j)$, $I_t(q_j)$ are the partial pixel intensity derivatives of the image I at the position (x, y) and time t, evaluated at point q_j. This system has more equations than unknowns and thus can be solved for the velocity vector (V_x, V_y). We used the inverse linear transformation matrix (M^{-1}) between frames to stabilize the video where a specific location on the slope remains in the same location in the video.

In the second step, we used principles of the Eulerian Video Magnification (Wu and others, 2012) to develop an Eulerian video detection method (EVD) to detect small pixel intensity changes at the snow surface. The EVD method involves the following steps: (1) applying a spatial decomposition – Gaussian pyramid (Burt and Adelson, 1983), (Fig. 3) to the video frames, (2) processing the low-resolution images by applying a temporal filter to the frame sequence, (3) applying the reversed spatial decomposition of step one and (4) detecting spatial and temporal changes in pixel intensity in the up-sampled bands (Fig. 4). We discuss each of these steps below.

A Gaussian Pyramid (Fig. 3) is a collection of images (all arising from a single original image) that are successively downsampled by removing every even-numbered row and column of pixels and convoluted with a Gaussian kernel (Eqn 2). To produce the layer I_{i+1} of image I in the Gaussian pyramid, we downsampled I_i and convoluted the down sampled image with the Gaussian kernel:

$$\frac{1}{16}\begin{bmatrix} 1 & 4 & 6 & 4 & 1 \\ 4 & 16 & 24 & 16 & 4 \\ 6 & 24 & 36 & 24 & 6 \\ 4 & 16 & 24 & 16 & 4 \\ 1 & 4 & 6 & 4 & 1 \end{bmatrix} \tag{2}$$

For our application, we used a three-layer pyramid. Applying a temporal filter on the top of the Gaussian Pyramid frame sequence instead of the original video allows us to reduce noise in the temporal axis and computation time, but it also reduces the sharpness of the video on the spatial scale.

https://doi.org/10.1017/aog.2023.36 Published online by Cambridge University Press

Figure 1. Comparison of enhanced (left) and original (right) frames extracted from a video of an avalanche from Alaska. We estimate that the crack in the weak layer was initiated at frame number 38. At frame number 37 (row A, 0.04 s. before crack initiation), snow surface movement from the snowboarder pushing the snow surface is visible up to 1.5 m downslope from the snowboarder. Frame number 47 (row B, 0.18 s. after crack initiation), snow surface movement is visible downslope from the snowboarder in the enhanced images (b1). Cracks on the snow surface below the snowboarder appear on frame 52 (c2, 0.28 s. after crack initiation), and snow surface movement becomes visible where the crown wall eventually develops to the left of the snowboarder (c1). In frame 56 (row D, 0.36 s. after crack initiation), the crown wall starts to appear on the snow surface in the original video (d2).

The main goal of the second step is to filter noise within the video data. Digital image noise is the unwanted and unpredictable fluctuation of image pixel values. Noise can be caused by various factors, including environmental factors like low light and temperature affecting the imaging sensor, dust particles in the scanner leading to dark or bright spots in the digital image, transmission channel interference resulting in bit errors or signal loss, variations in the sensitivity of the individual pixels in the camera's

https://doi.org/10.1017/aog.2023.36 Published online by Cambridge University Press

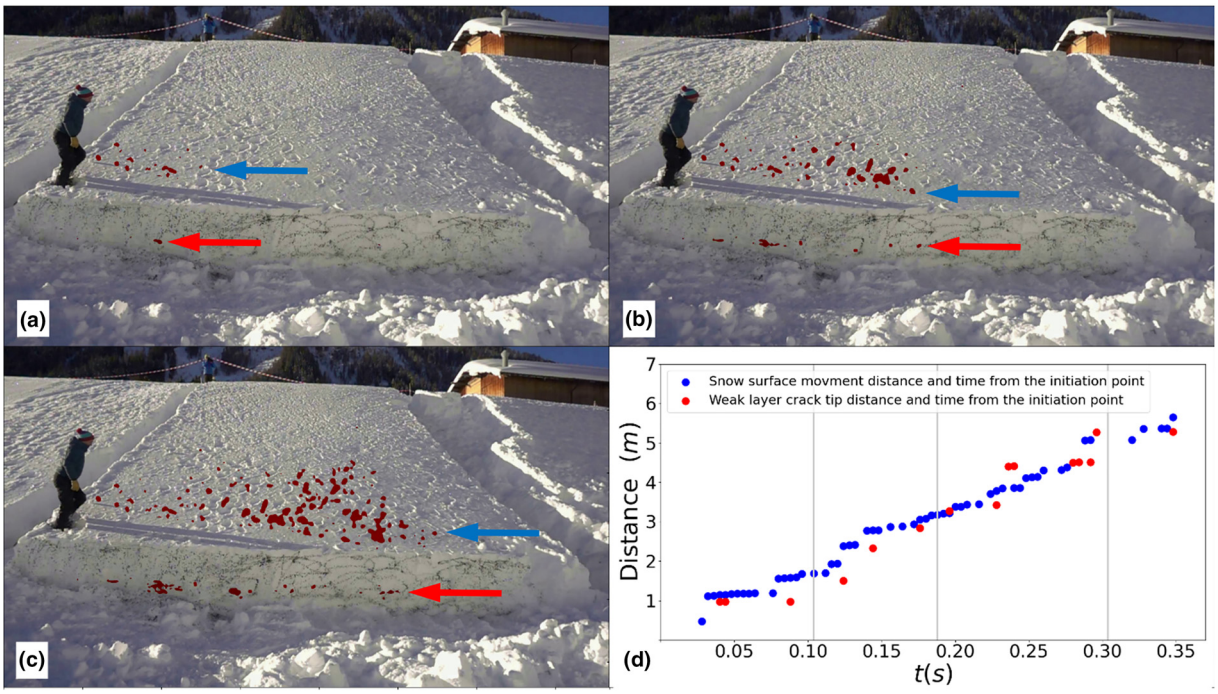

Figure 2. A sequence of of a 10 m by 10 m small avalanche experiment video frames where both snow surface movements (marked in blue arrow) and weak layer cracks have been detected (marked in red arrow) after 0.1 s (a), 0.18 s (b) and 0.3 s (c). (d) distance and time from the initiation point and time for both detected snow surface motion (blue) and detected weak layer crack tip (red). The gray vertical lines in D show the time of frames A, B and C.

Figure 3. Gaussian pyramid, where subsequent images are weighted down using a Gaussian average on each pixel and scaled down by a factor of 2 along each coordinate direction or scaled up by preforming the inverse scaled down Gaussian pyramid operation.

sensor leading to fixed pattern noise, natural fluctuations in light causing random noise, and electronic circuit noise originating from the image sensor and circuitry of a digital camera (Romberg and others, 1999; Boyat and Joshi, 2015 and Swamy and Kulkarni, 2020).

Using Fast Fourier Transform (Cooley and Tukey, 1965) on the portion of the video from the initiation to the appearance of surface cracks and Inverse Fast Fourier Transformations, we filtered out frequencies outside the period between crack initiation and the initial appearance of cracks (Eqn 4) on the snow surface in the video. The Fourier coefficient c_k for the k^{th} Fourier coefficient for every location pixel in the N frames pyramid is the sum:

$$c_k = \sum_{n=0}^{N-1} I_n \cdot e^{-2\pi i(kn/N)} \tag{3}$$

where I_n is the video's pixel intensity for every location on the pyramid video sequence, n is index of the Gaussian pyramid frames from the video sequence from initiation to when cracks on the snow surface become visible, N is the number of video frames from the crack initiation to when surface cracks are visible, and k, is the discrete Fourier coefficient index, $k \in \{0, 1, 2, \ldots, N\}$.

We assume that the surface movement is due to crack propagation in the weak layer. Since these movements occur only between the times a crack is initiated and the appearance of surface cracks, we filtered out noise in the video by zeroing all the Fourier coefficients associated with higher frequencies as follows:

$$c_k = \begin{cases} c_k, & if\ k < 2N \cdot fps \\ 0, & \text{otherwise} \end{cases} \tag{4}$$

https://doi.org/10.1017/aog.2023.36 Published online by Cambridge University Press

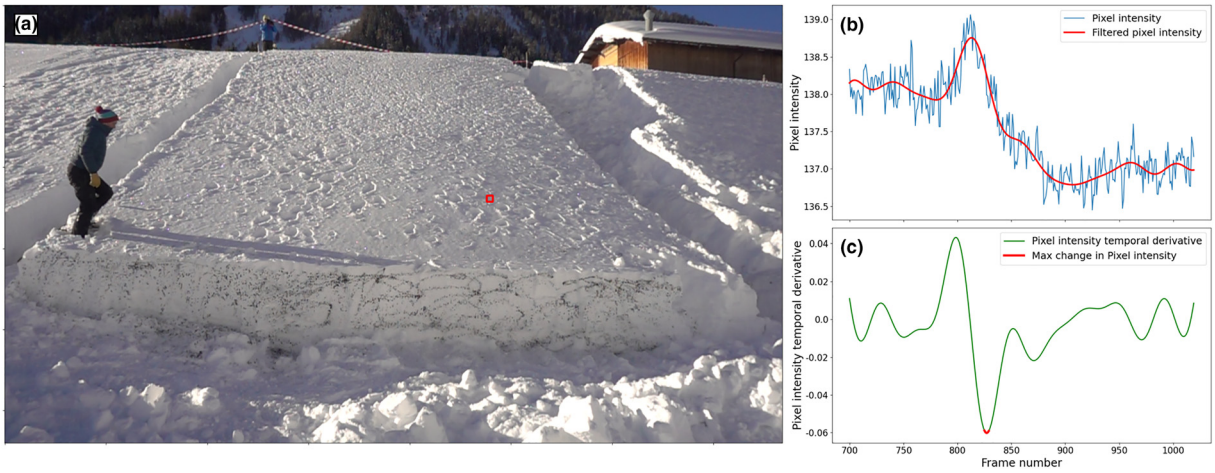

Figure 4. (a) A video frame of a 10 m by 10 m small avalanche experiment. (b) The mean pixel intensity (in blue) and the filtered signal (in red) of the pixels in the red rectangle. (c) The first temporal derivative of the filtered pixel intensity signal. The derivative minima (red dot) at frame 828 represented when the weak layer's crack passed below the area marked with the red rectangle. Both (b) and (c) share the same *x*-axis.

where *fps* is the frame rate of the video. The reconstructed pixel intensity function $I_r(n)$ for every frame $n \in \{0, 1, 2, \ldots, N\}$, for every pixel in the down-sampled pyramid is:

$$I_r(n) = \frac{1}{N}\sum_{k=0}^{N-1} c_k \cdot e^{2\pi i(nk/N)} \tag{5}$$

Using a Gaussian Pyramid, we then up-sample $I_r(n)$ to the original pixel locations in the original video. Finally, we compare the pixel intensity with the temporal derivative ($\mathrm{d}I_r/\mathrm{d}t$) to capture the time when the significant changes in pixel intensity occurred. To avoid capturing noise in locations where our method does not detect actual snow surface movements, we selected a time (t) where the temporal second derivative value where equal to zero ($(\partial^2 I_r/\partial^2 t) = 0$), and the first temporal derivative value is also an outlier (outside three times the standard deviation) (Fig. 4).

Crack speed estimates and analysis

For one of our avalanche videos (Switzerland1), we had the exact location of the avalanche. We geo-located the avalanche slope, using its location to derive the distances from the crack initiation to the detected locations of slab motion. Unfortunately, we did not have the avalanche location or the camera's intrinsic parameters for the other four videos. We did not see obvious lens distortion in our videos as the camera scene moved across the slope. However, we did incorporate the *possibility* of lens distortion in our error estimates for our distance measurements.

To estimate the distance from crack initiation to other points on the slope in these four avalanches, we estimated the skier/snowboarder height to be 1.75 m. We calculated the distances between different locations on the slope by comparing these distances in pixels to the size of the snowboarder in pixel units. We estimate our distance measurements error to be ±10 pixels and our time error to be ±two video frames. In each video, we selected only locations where the detected movement appeared before the appearance of cracks on the snow surface. In addition, we assume that the crack tips travel away from the initiation point; thus, we omitted the detected location that appeared in the same direction as the initiation point after another detected location further away.

To differentiate between slope and cross-slope crack propagation directions, we use the direction of the avalanche flow in the starting zone as the downslope direction. We considered propagation in direction to detected points within 45° of the slope direction (up or down) as slope direction and the rest as cross-slope direction.

Our analysis also differentiated between hard and soft slab avalanches. As a rough measure, we considered an avalanche to be a hard slab when avalanche debris blocks remained larger than a third of a person while traveling through the avalanche starting zone. We classified the rest of the avalanches as soft slabs.

To ensure that our analysis is not skewed toward avalanches with more estimates, we used the mean estimates in slope and cross-slope directions per avalanche.

Method verification

We verified the accuracy of our method by comparing speed estimates to measurements from two PSTs analyzed with PTV (Crocker and Grier, 1996; van Herwijnen and others, 2016) (Fig. 5), one PST assessed using DIC (Fig. 6), and one small avalanche experiment. In the small avalanche we compared the EVD of the snow surface with the DIC-based displacement field of the sidewall (Bergfeld and others, 2018, 2021). Furthermore, we validate our EVD approach by comparing it with two other MPM simulation of physically-based render (PBR) with Houdini software: a 30 m long PST and avalanche. These PBR simulations allow us to accurately locate the crack tip and provide additional means to verify the effectiveness of our method (Fig. 7). (Table 1).

Results

Method verification

To measure crack speed from snow surface movements, we detected pixel intensity changes due to slab movement, which are likely at or closely behind the weak layer crack propagation tip. We compared our method to field experiments where we measured crack speeds with PTV or DIC to verify our method. We also tracked EVD surface movement along with EVD of the weak layer fracturing in one video of a 10 by 10 m avalanche experiment , as well as in some MPM simulations of PSTs and a simulated avalanche (Trottet and others, 2022). Crack speed estimates based on our EVD method are quite similar to speeds obtained with these other methods (Figs 5–7 and Table 1). In fact, in all field experiments and MPM simulations, the speed differences were within 10% (Table 1).

https://doi.org/10.1017/aog.2023.36 Published online by Cambridge University Press

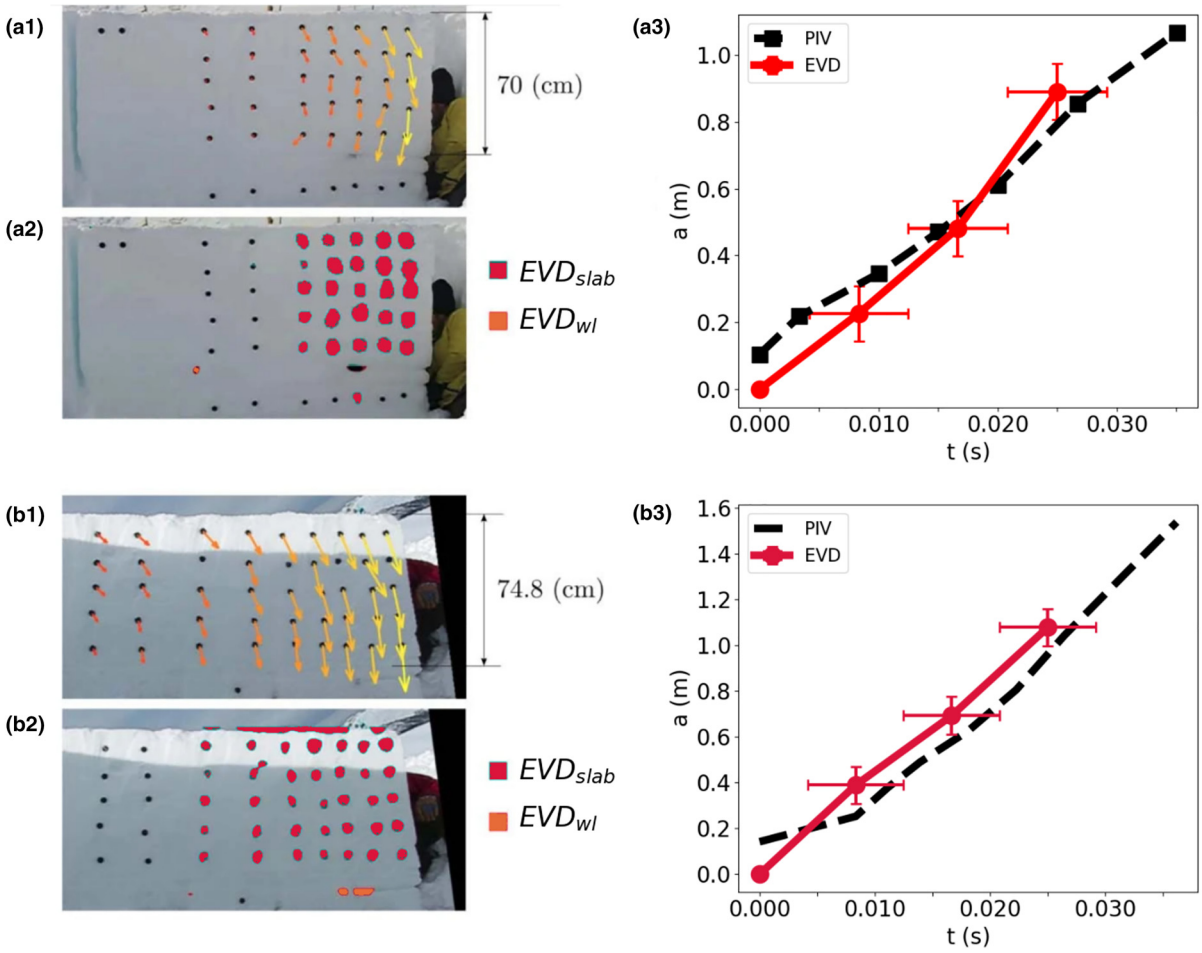

Figure 5. (a) Application of the EVM method to field experiments and comparison with results obtained with particle tracking velocimetry (PTV). (a1) PTV results for a flat (0° slope) field PST. (a2) corresponding EVD. (a3) Crack tip position with time-based from PTV (black) and EVD (red). (b) same as (a) for a PST on a 37° slope.

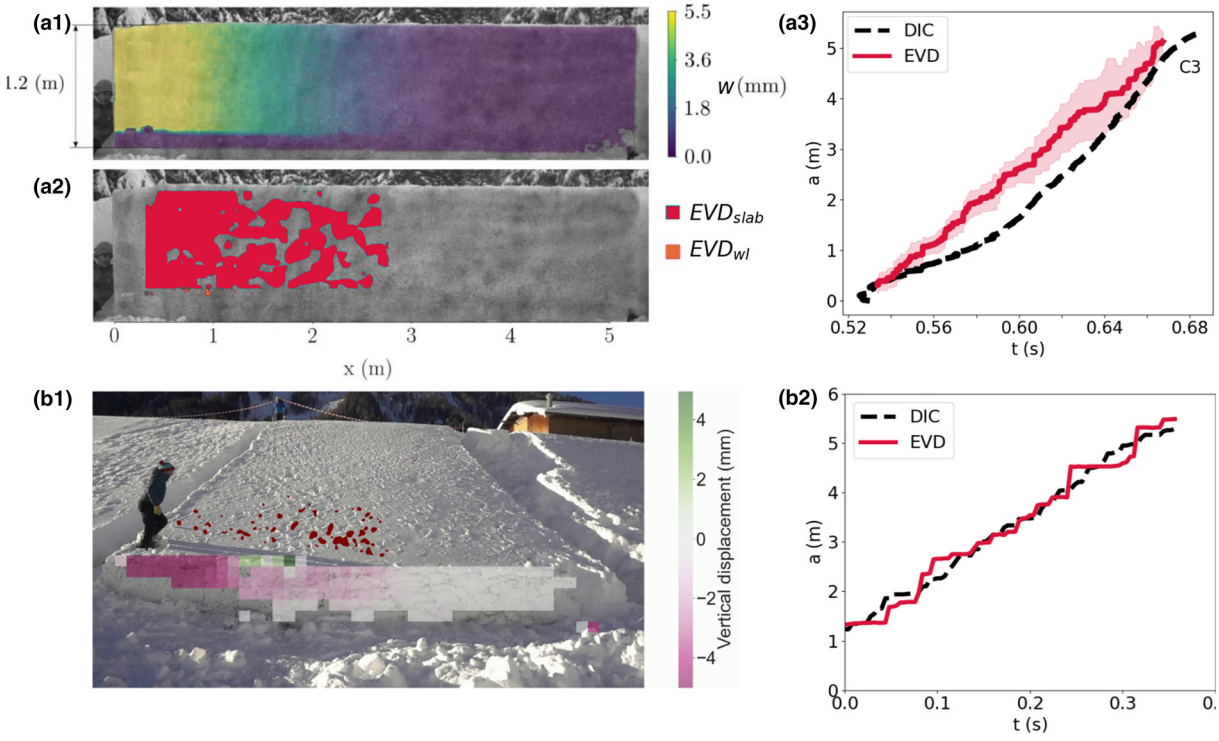

Figure 6. (a) Digital Image Correlation (DIC). (a1) PTV results for a flat (0° slope) field PST. (a2) corresponding EVD. (a3) Crack tip position with time-based from DIC (black) and EVD (red). (b1) EVD results on the snow surface (red) on an experiment on a small isolated slope. DIC results for the sidewall facing the camera (colors). (b2) Crack tip position with time from DIC (black) and EVD (red).

https://doi.org/10.1017/aog.2023.36 Published online by Cambridge University Press

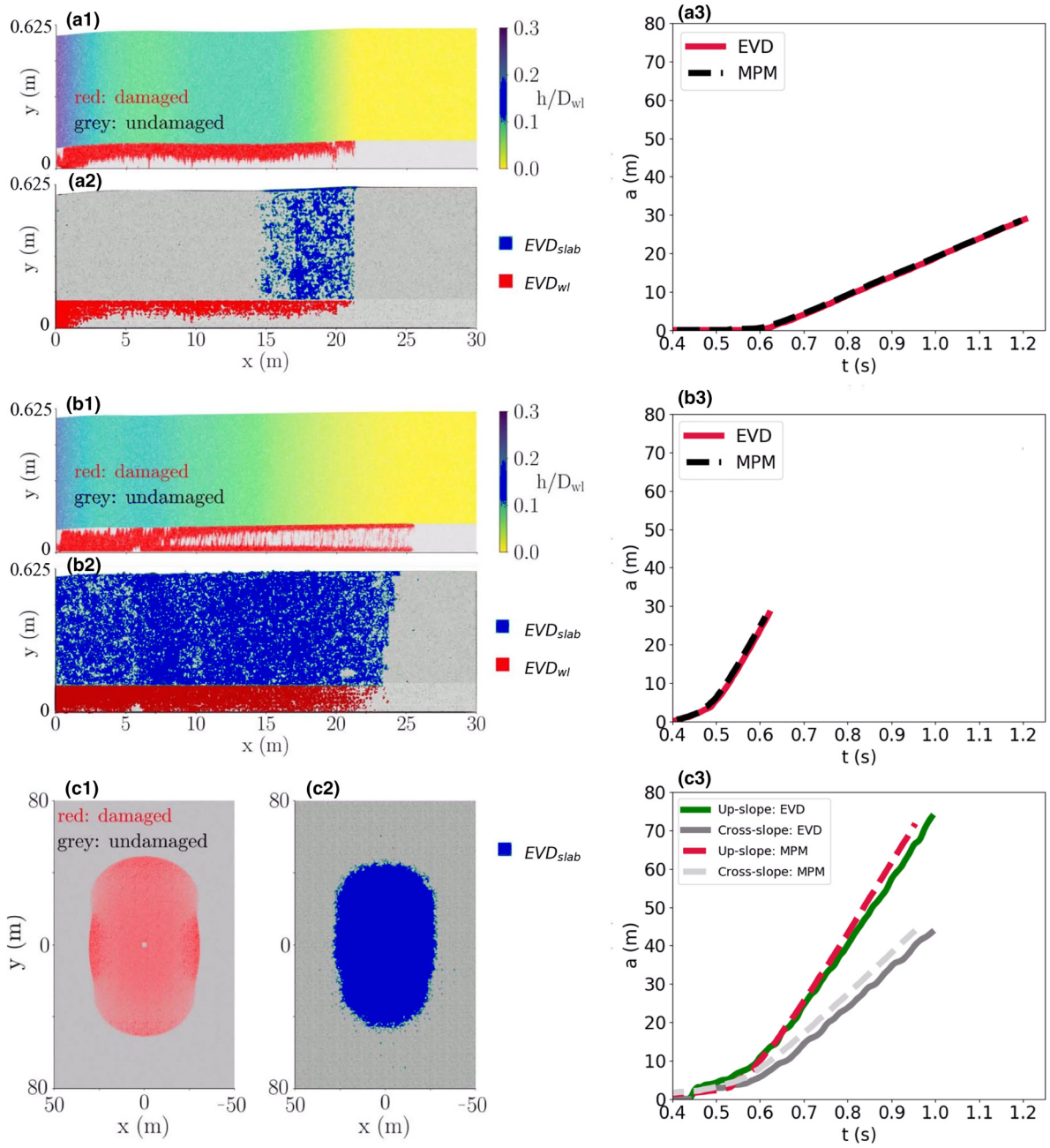

Figure 7. (a1) MPM simulation of a 30 m PST on flat terrain, (a2) EVD results for the simulation, and (a3) crack tip position with time-based on MPM (red) and EVM (blue). (b) Same as a) except on a 30° slope. (c1) MPM 2D MPM simulation of an avalanche on 30 degrees slope, (c2) EVD results for the simulation, and (c3) crack tip position with time-based from MPM and EVD in both slope and cross-slope directions.

Slope-scale crack speed estimates

We analyzed five skier or snowboarder-triggered avalanches, three with hard slabs and two with soft slabs. Slab hardness and the direction of crack propagation with respect to the slope affected weak layer crack speeds. We observed snow surface movement rapidly advancing in the up- and down-slope directions (Fig. 8) with slower snow surface movement in the cross-slope direction. Crack speeds in the slope direction averaged 135 m s^{-1}, while cross-slope crack speeds are considerably lower, averaging

Table 1. Characteristics and results of field experiments and MPM simulations used to validate our EVM crack speed estimates

Test	Type	Length m	Slope °	FPS	Pixel/m	Mean Test m s^{-1}	Mean EVD speed
PST Field Test (PIV)	Field Test	1.10	0	120	0.0034	28.1	31.1
PST Field Test (PIV)	Field Test	1.60	37	120	0.0033	39.5	38.44
PST Field Test (PIV)	Field Test	5	0	7000	0.0041	33.0	34.9
Small avalanche test (DIC)	Field Test	10	30	250	0.0675	28.6	29.5
PST MPM simulation	Simulation	30	0	240	0.026	33.1	32.9
PST MPM simulation	Simulation	30	30	240	0.026	84.5	84.63
Avalanche MPM upslope	Simulation	80	30	240	0.067	82.6	79.5
Avalanche MPM cross slope	Simulation	50	30	240	0.074	49.1	44.5

https://doi.org/10.1017/aog.2023.36 Published online by Cambridge University Press

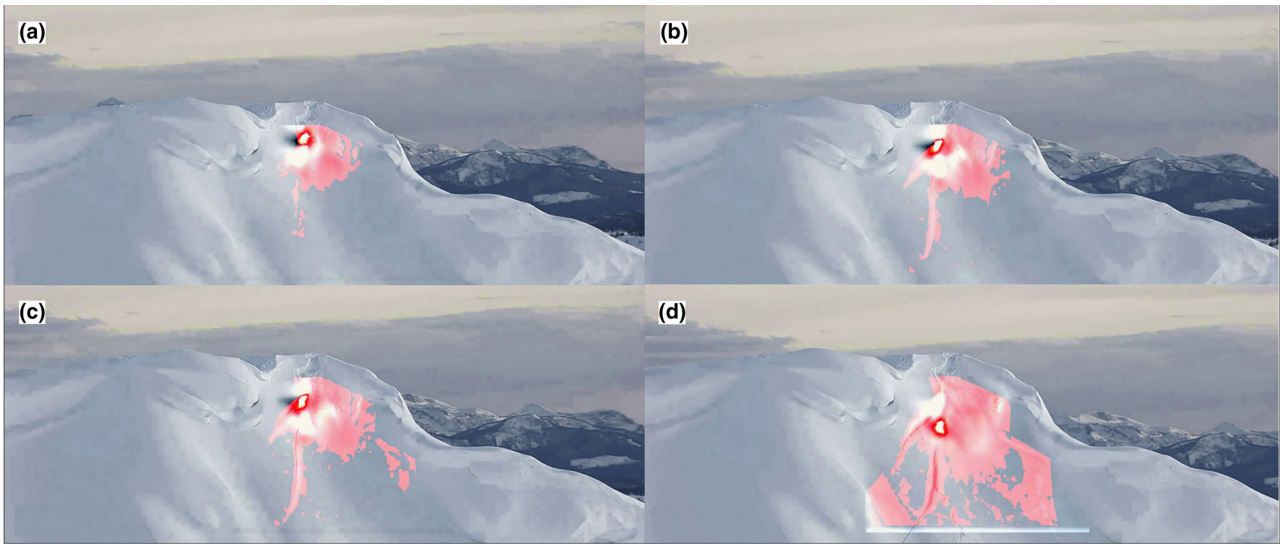

Figure 8. A sequence of video frames of avalanche release. In red are the locations where we detected snow surface movement up to the time of the frame. Initially (A and B), weak layer crack propagation can only be detected advancing downslope from the snowboarder. As larger areas of the weak layer fractured downslope from the snowboarder, crack propagation advances in the cross-slope direction.

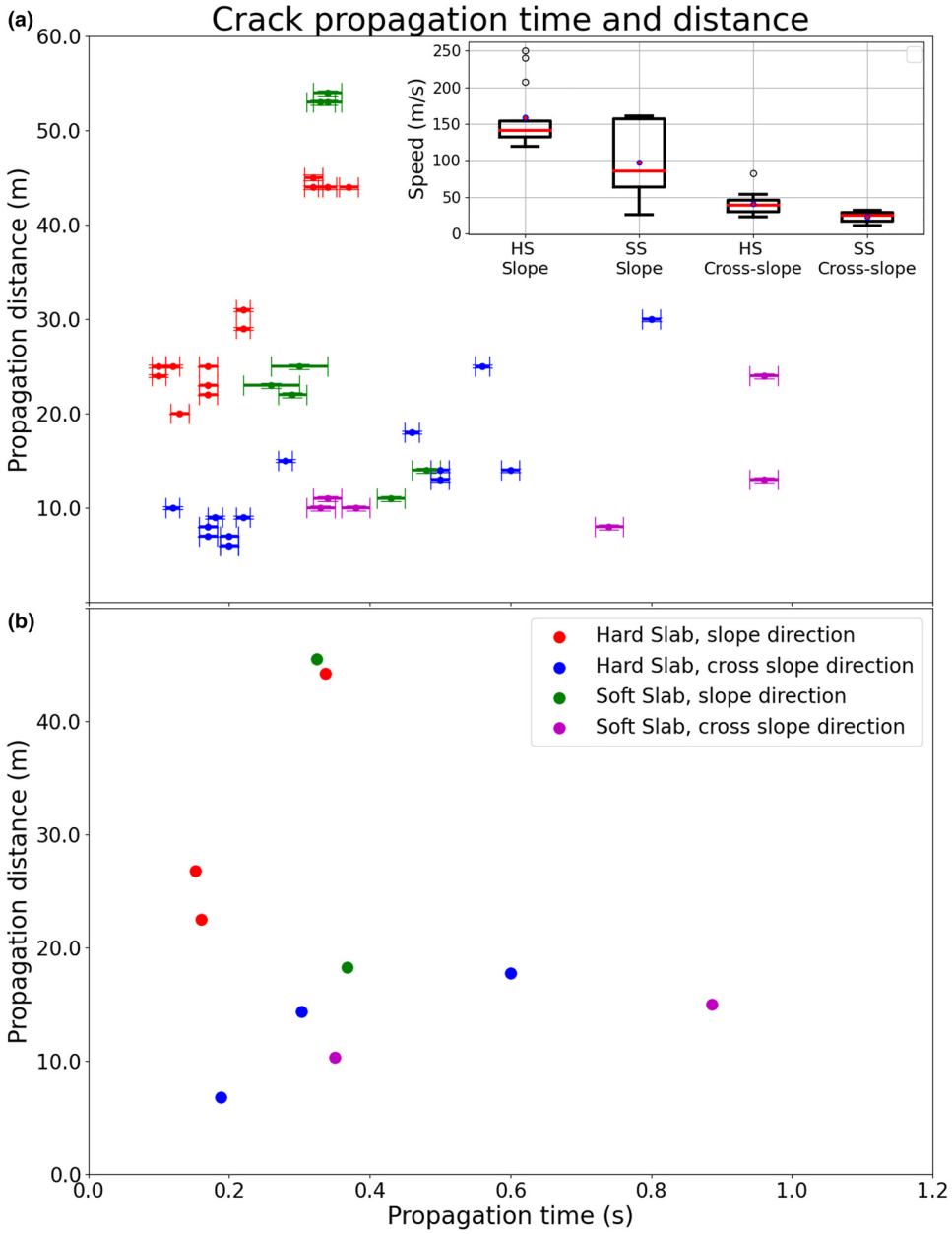

Figure 9. Color-codded estimates of crack propagation time and distance. (a) Representation for each estimate ($n = 42$), with the insert showing the speed estimate distribution for slope and cross-slope propagation for hard and soft slabs from all 42 estimates. (b) Representation of the mean values for each avalanche. Both Figures A and B show a similar trend of faster propagating cracks in the slope direction in comparison to the cross-slope direction and faster-propagating cracks under harder slabs.

https://doi.org/10.1017/aog.2023.36 Published online by Cambridge University Press

35 m s^{-1}. Thus, slope-direction crack speeds averaged nearly four times faster than cross-slope crack speeds (Fig. 9). Mean estimated crack speeds in hard slab avalanches were 1.6 and 1.7 times faster than soft slab avalanches in cross-slope and slope directions, respectively (Fig. 9). We did have two notable outliers in our down-slope crack speeds, with estimates of 26 and 29 m s^{-1}. However, these estimates were less than 15 m from the crack initiation point. Our measurements (Table 2) suggest that down-slope crack speeds close to the initiation point (within about 15 m) and cross-slope crack speeds align reasonably well with previous speed estimates measured for PSTs and whumpfs (van Herwijnen, 2005; Bair and others, 2014; van Herwijnen and Birkeland, 2014; van Herwijnen and others, 2016; Bergfeld and others, 2021; Bergfeld and others, 2022), and cross-slope speeds estimated for larger avalanches (Bergfeld and others, 2022).

In two of the videos, we estimated crack propagation speeds in several locations between the initiation point and the boundary of the release area. We estimated the slab to be soft; in both videos, the avalanche trigger was a snowboarder making a turn. In both videos, the crack speed in the downslope direction increased with distance (Fig. 10).

We classified two avalanches as 'soft slabs' and three as 'hard slabs.' In total, we had 21 slope-direction crack speed estimates of the hard slab and 21 cross-slope direction crack speed estimates of soft slab avalanches. Average crack speeds were higher for our hard slabs (158 m s^{-1}) than for soft slabs (97 m s^{-1}). The cross-slope crack speeds between the two groups also varied, averaging 40 m s^{-1} for hard slabs and 23 m s^{-1} for soft slabs.

Discussion

Our results comparing up- and down-slope crack speed estimates to cross-slope estimates support the idea that different crack propagation regimes drive propagation on flat, up- and down-slope and cross-slope directions. Further evidence is provided by comparing up- and down-slope crack speeds close to the initiation point to crack speeds farther from the initiation point. Our crack speed estimates within about 15 m of the initiation point – regardless of slope orientation – are about 27 ± 2 m s^{-1}, aligning closely with previous crack speed estimates of PSTs and whumps, which range from 17 to 42 m s^{-1} (Jamieson and Johnston, 1992; van Herwijnen and Jamieson, 2005; Bair and others, 2014; van Herwijnen and Birkeland, 2014; van Herwijnen and others, 2016; Bergfeld and others, 2021). At distances, farther than 15 m from the initiation point, speeds up and down-slope greatly exceed cross-slope speeds. Here our up- and down-slope crack speeds averaged 143 ± 27 m s^{-1}, nearly four times faster than the mean cross-slope speeds. These higher estimates are consistent with the upper end of previous slope scale estimates by

Table 2. All estimates from the five videos

ID	Location	Slab hardness	Trigger	Direction	Distance m	Time s	Speed m s^{-1}
1	Alaska1	Soft	Snowboarding	Downslope	11 ± 0.25	0.43 ± 0.02	26 ± 2.1
2	Alaska1	Soft Slab	Snowboarding	Downslope	14 ± 0.25	0.48 ± 0.02	29 ± 2.0
3	Alaska1	Soft Slab	Snowboarding	Downslope	23 ± 0.25	0.26 ± 0.04	88 ± 17.7
4	Alaska1	Soft Slab	Snowboarding	Downslope	25 ± 0.25	0.3 ± 0.04	83 ± 14.1
5	Alaska1	Soft Slab	Snowboarding	Cross slope	24 ± 0.25	0.96 ± 0.02	25 ± 0.8
6	Alaska1	Soft Slab	Snowboarding	Cross slope	8 ± 0.25	0.74 ± 0.02	11 ± 0.8
7	Alaska1	Soft Slab	Snowboarding	Cross slope	13 ± 0.25	0.96 ± 0.02	14 ± 1.0
8	Switzerland1	Hard Slab	Landing	Downslope	24 ± 0.15	0.1 ± 0.01	240 ± 28.3
9	Switzerland1	Hard Slab	Landing	Downslope	25 ± 0.15	0.1 ± 0.01	250 ± 29.4
10	Switzerland1	Hard Slab	Landing	Downslope	25 ± 0.15	0.12 ± 0.01	208 ± 20.6
11	Switzerland1	Hard Slab	Landing	Cross slope	10 ± 0.15	0.12 ± 0.01	83 ± 9.3
12	Switzerland1	Hard Slab	Landing	Cross slope	9 ± 0.15	0.18 ± 0.01	50 ± 3.8
13	Switzerland1	Hard Slab	Landing	Downslope	29 ± 0.15	0.22 ± 0.01	132 ± 6.8
14	Switzerland1	Hard Slab	Landing	Downslope	31 ± 0.15	0.22 ± 0.01	141 ± 7.3
15	Switzerland1	Hard Slab	Landing	Cross slope	9 ± 0.15	0.22 ± 0.01	41 ± 2.6
16	Switzerland1	Hard Slab	Landing	Cross slope	15 ± 0.15	0.28 ± 0.01	54 ± 2.8
17	Switzerland1	Hard Slab	Landing	Cross slope	18 ± 0.15	0.46 ± 0.01	39 ± 1.3
18	Switzerland1	Hard Slab	Landing	Cross slope	25 ± 0.15	0.56 ± 0.01	45 ± 1.4
19	France	Hard Slab	Skiing	Downslope	20 ± 0.024	0.13 ± 0.013	154 ± 17.1
20	France	Hard Slab	Skiing	Downslope	23 ± 0.024	0.17 ± 0.013	135 ± 11.6
21	France	Hard Slab	Skiing	Downslope	22 ± 0.024	0.17 ± 0.013	129 ± 11.3
22	France	Hard Slab	Skiing	Downslope	25 ± 0.024	0.17 ± 0.013	147 ± 12.4
23	France	Hard Slab	Skiing	Cross slope	7 ± 0.024	0.17 ± 0.013	41 ± 3.7
24	France	Hard Slab	Skiing	Cross slope	8 ± 0.024	0.17 ± 0.013	47 ± 4.1
25	France	Hard Slab	Skiing	Cross slope	6 ± 0.024	0.2 ± 0.013	30 ± 2.2
26	France	Hard Slab	Skiing	Cross slope	6 ± 0.024	0.2 ± 0.013	30 ± 2.2
27	France	Hard Slab	Skiing	Cross slope	7 ± 0.024	0.2 ± 0.013	35 ± 2.6
28	Switzerland2	Hard Slab	Landing	Upslope	44 ± 0.2	0.34 ± 0.013	129 ± 6.2
29	Switzerland2	Hard Slab	Landing	Upslope	44 ± 0.2	0.37 ± 0.013	119 ± 4.8
30	Switzerland2	Hard Slab	Landing	Upslope	44 ± 0.2	0.32 ± 0.013	138 ± 6.5
31	Switzerland2	Hard Slab	Landing	Upslope	45 ± 0.3	0.32 ± 0.013	141 ± 6.8
32	Switzerland2	Hard Slab	Landing	Cross slope	14 ± 0.2	0.5 ± 0.013	28 ± 1.2
33	Switzerland2	Hard Slab	Landing	Cross slope	13 ± 0.2	0.5 ± 0.013	26 ± 1.1
34	Switzerland2	Hard Slab	Landing	Cross slope	14 ± 0.2	0.6 ± 0.013	23 ± 1.2
35	Switzerland2	Hard Slab	Landing	Cross slope	30 ± 0.2	0.8 ± 0.013	38 ± 1.3
36	Alaska2	Soft Slab	Snowboarding	Downslope	22 ± 0.25	0.29 ± 0.02	76 ± 6.4
37	Alaska2	Soft Slab	Snowboarding	Downslope	53 ± 0.25	0.33 ± 0.02	161 ± 10.8
38	Alaska2	Soft Slab	Snowboarding	Downslope	53 ± 0.25	0.34 ± 0.02	156 ± 10.4
39	Alaska2	Soft Slab	Snowboarding	Downslope	54 ± 0.25	0.34 ± 0.02	159 ± 10.5
40	Alaska2	Soft Slab	Snowboarding	Cross slope	10 ± 0.25	0.33 ± 0.02	30 ± 3.1
41	Alaska2	Soft Slab	Snowboarding	Cross slope	11 ± 0.25	0.34 ± 0.02	32 ± 3.2
42	Alaska2	Soft Slab	Snowboarding	Cross slope	10 ± 0.25	0.38 ± 0.02	26 ± 2.5

https://doi.org/10.1017/aog.2023.36 Published online by Cambridge University Press

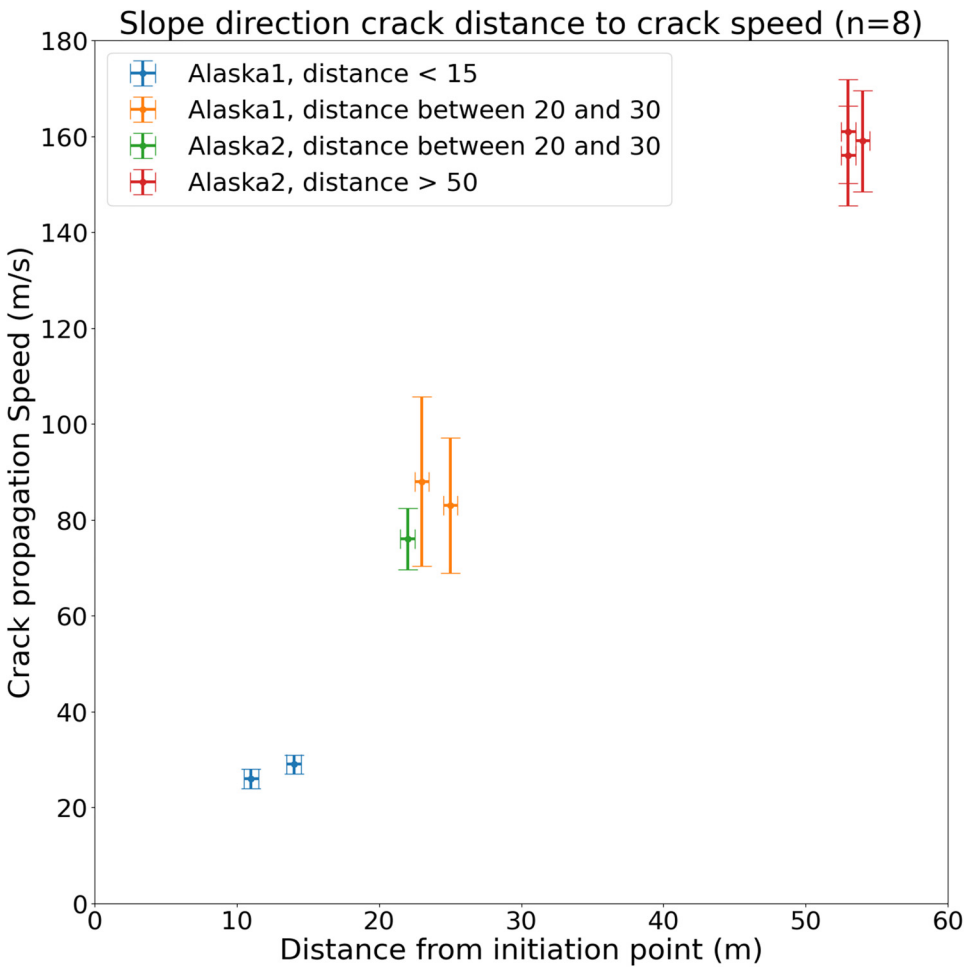

Figure 10. Crack propagation speed against crack propagation distance from two videos of a snowboarder-triggered soft slab avalanche (Table 2, Alaska1 and Alaska2), where we could estimate the propagation speed in several distances in one avalanche. The different colors are for the two different avalanches and for different distances from the trigger point of the slide.

Hamre and others (2014), which were based on surface cracks and could, therefore, only assess speeds well away from trigger points. Our results thus support the recent work by Trottet and others (2022) and Bobillier and others (2023), who proposed that cracks propagate as sub-Rayleigh anticracks close to initiation points before transitioning to a much faster supershear mode in the up- and down-slope directions. Cross-slope cracks are mode III fractures, which in theory, have their speeds limited by the slab's flexural wave speed (Burridge, 1973; Bergfeld and others, 2021).

Our results also suggest faster slope-scale crack speeds with harder – and presumably denser – slabs (Fig. 9; Table 2). This finding is consistent with previous field measurements with PSTs (van Herwijnen and Birkeland, 2014; van Herwijnen and others, 2016; Birkeland and others, 2019), and it also provides field verification for numerical simulations of Trottet and others (2022) and Bobillier and others (2023). In addition, our results from two avalanches show that cracks with higher propagation speeds travel over larger distances than cracks with lower propagation speeds (Fig. 10). This is in line with video analasys of PST (van Herwijnen and others, 2016).

Since we estimated crack speeds from videos, our methods have limitations. First, our speeds are not direct measurements. Rather, we use snow surface movement as a proxy for crack tip location. Second, crack distances for four of our five avalanche videos are estimated from the snowboarder/skier's height and not from direct measurements. Third, our method does not always detect the crack tip location; as a result, most of our estimates are bulk estimates and not point estimates. Fourth, we estimated speed from only five avalanches, though we did ensure an even contribution of all the avalanches when comparing crack speed trends between hard and soft slabs, and between slope-parallel and cross-slope directions. Fifth, our speed analysis in Figure 9(A) relies on all 42 estimates and may show some bias toward avalanches with a larger number of speed estimates. Finally, we found that our method did not work on videos taken on cloudy days, so we could not adequately analyze videos taken in cloudy conditions. Conversely, avalanche videos on slopes with pixel over saturation may not be suitable for EVD as changes in the snow surface will remain outside of the pixel intensity range. For videos where small areas of the slope have over-saturated pixel intensities, the EVD can detect snow surface movements around these areas. Videos with large slope areas with over-saturated pixel intensities may not be suitable for the EVD methods.

Apart from the limitations already highlighted, further research is necessary to gain a more comprehensive understanding of the lightning prerequisites of our method. To this end, it would be interesting to explore the effects of different lighting conditions on avalanche simulations, encompassing visual rendering of both direct and diffuse simulated light sources. This would enable us to gain a deeper insight into the performance and accuracy of our approach under varying lighting conditions.

For this work, we analyzed videos featuring snow surfaces with varying textures. Notably, we observed that the texture of the snow surface had no impact on the effectiveness of our approach in detecting snow surface motion. Specifically, the snow surface in the small-scale avalanche experiment featured a strong texture, while the surfaces in all five avalanche videos were relatively smooth, and this difference appeared to affect the accuracy of our method.

Despite the limitations, our technique verified quite well with previous techniques for measuring crack speeds (Figs 5–7;

https://doi.org/10.1017/aog.2023.36 Published online by Cambridge University Press

Table 1). This gives us confidence that our methods will enable researchers to better investigate and understand weak layer crack propagation under actual slope-scale avalanches. Combining our novel video analysis technique with additional field measurements of snowpack properties may help us predict slope-scale crack speeds, and that information might allow us better to predict propagation distance and the size of expected avalanches.

Conclusions

We present a novel method for tracking snow surface movement in the early stages of dry slab avalanche release. Unlike previous video analyses of slope scale crack propagation, our method tracks snow surface movement over time and space *before* surface cracks are visible. It relies on the change in frame pixel intensity to infer the position of the crack tip in the weak layer. The method has been validated based on field experiments and numerical simulations. Our estimates show that crack speeds vary with the direction of propagation with respect to the slope and slab hardness. It also shows that without terrain limitations, cracks propagating at higher speeds travel over larger distances in avlanches' start zones. Our work is an important step toward a better understanding of fracture processes involved in dry-snow slab avalanche release at the slope scale.

Acknowledgements. We want to thank Melin Walet for her help with the DIC analysis of the small avalanche experiment. We also thank Ned Bair and an anonymous reviewer for their helpful comments on our paper.

Data. We did not get permission to share all the videos we used for this work. The original videos and the highlighted detected snow surface motion videos can be found at https://github.com/ronimos/Crack-Speed-Videos

References

Bair EH, Simenhois R, van Herwijnen A and Birkeland KW (2014) The influence of edge effects on crack propagation in snow stability tests. *The Cryosphere* **8**(4), 1407–1418.

Bergfeld B, van Herwijnen A, Dual J and Schweizer J (2018) Dynamic crack propagation in weak snowpack layers: insights from high-resolution, high-speed photography. Proceedings of the International Snow Science Workshop, Innsbruck, Austria, 2018.

Bergfeld B and 5 others (2021) Dynamic crack propagation in weak snowpack layers: insights from high-resolution, high-speed photography. *The Cryosphere* **15**(7), 3539–3553.

Bergfeld B and 9 others (2022) Crack propagation speeds in weak snowpack layers. *Journal of Glaciology* **68**(269), 557–570.

Bergfeld B and 7 others (2023) Temporal evolution of crack propagation characteristics in a weak snowpack layer: conditions of crack arrest and sustained propagation. *Natural Hazards and Earth System Sciences* **23**(1), 293–315. doi: 10.5194/nhess-23-293-2023.

Birkeland KW, Van Herwijnen A, Reuter B and Bergfeld B (2019) Temporal changes in the mechanical properties of snow related to crack propagation after loading. *Cold Regions Science and Technology* **159**, 142–152. doi: 10.1016/j.coldregions.2018.11.007.

Bobillier G and 5 others (2023) Numerical investigation of crack propagation regimes in snow fracture experiments. *Granul. Matter, in review.*

Boyat AK and Joshi BK (2015) A Review Paper: Noise Models in Digital Image Processing. ArXiv. /abs/1505.034.

Broberg KB (1996) How fast can a crack go? *Materials Science* **32**(1), 80–86.

Burridge R (1973) Admissible speeds for plane-strain self-similar shear cracks with friction but lacking cohesion. *Geophysical Journal International* **35**, 439–455.

Burt P and Adelson E (1983) The Laplacian pyramid as a compact image code. *IEEE Transactions on Communications* **31**(4), 532–540. doi: 10.1109/TCOM.1983.1095851

Cooley JW and Tukey JW (1965) An algorithm for the machine calculation of complex Fourier series. *Mathematics of Computation* **19**(90), 297–301.

Crocker JC and Grier DG (1996) Methods of digital video microscopy for colloidal studies. *Journal of Colloid and Interface Science* **179**(1), 298–310.

Gaume J, Gast T, Teran J, van Herwijnen A and Jiang C (2018) Dynamic anticrack propagation in snow. *Nature Communications* **9**(1), 1–10.

Gaume J, van Herwijnen A, Chambon G, Birkeland KW and Schweizer J (2015) Modeling of crack propagation in weak snowpack layers using the discrete element method. *The Cryosphere* **9**(5), 1915–1932.

Gaume J, van Herwijnen A, Gast T, Teran J and Jiang C (2019) Investigating the release and flow of snow avalanches at the slope-scale using a unified model based on the material point method. *Cold Regions Science and Technology* **168**, 102847.

Gauthier D and Jamieson B (2006) Towards a field test for fracture propagation propensity in weak snowpack layers. *Journal of Glaciology* **52**(176), 164–168.

Gross D and Seelig T (2017) *Fracture Mechanics: With an introduction to Micromechanics*. Berlin, Germany: Springer.

Hamre D, Simenhois R and Birkeland K (2014) Fracture speeds of triggered avalanches. In Proceedings ISSW, 174–178.

Heierli J (2005) Solitary fracture waves in metastable snow stratifications. *Journal of Geophysical Research: Earth Surface* **110**, F2.

Heierli J, Gumbsch P and Zaiser M (2008) Anticrack nucleation as triggering mechanism for snow slab avalanches. *Science* **321**(5886), 240–243.

Jamieson JB and Johnston CD (1992) Snowpack characteristics associated with avalanche accidents. *Canadian Geotechnical Journal* **29** (5), 862–866.

Johnson BC, Jamieson JB and Stewart RR (2004) Seismic measurement of fracture speed in a weak snowpack layer. *Cold Regions Science and Technology* **40**(1-2), 41–45.

Lucas BD and Kanade T (1981) An iterative image registration technique with an application to stereo vision. In IJCAI'81: 7th international joint conference on Artificial intelligence (Vol. 2, pp. 674–679).

McClung DM (2005) Approximate estimates of fracture speeds for dry slab avalanches. *Geophysical Research Letters* **32**(8).

Romberg JK, Choi H and Baraniuk RG (1999) Bayesian wavelet-domain image modeling using hidden Markov trees. In Proceedings 1999 International Conference on Image Processing (Cat. 99CH36348) (Vol. 1, pp. 158–162). IEEE.

Schweizer J, Jamieson JB and Schneebeli M (2003) Snow avalanche formation. *Reviews of Geophysics* **41**(4).

Schweizer J, Reuter B, van Herwijnen A, Richter B and Gaume J (2016) Temporal evolution of crack propagation propensity in snow in relation to slab and weak layer properties. *The Cryosphere* **10**(6), 2637–2653.

Shi J and Tomasi C (1994) Good features to track. (1994). Proceedings of IEEE Conference on Computer Vision and Pattern Recognition, 593–600.

Swamy S and Kulkarni PK (2020) A basic overview on image denoising techniques. *International Research Journal of Engineering and Technology* **7**(5), 850–857.

Trottet B, Simenhois R, Bobillier G *et al.* (2022) Transition from sub-Rayleigh anticrack to supershear crack propagation in snow avalanches. *Nature Physics* **18**, 1094–1098. https://doi.org/10.1038/s41567-022-01662-4

van Herwijnen AF (2005) Fractures in weak snowpack layers in relation to slab avalanche release. University of Calgary, Calgary, AB. doi: 10.11575/PRISM/15350

van Herwijnen A and 6 others (2016) Measuring the mechanical properties of snow relevant for dry-snow slab avalanche release using particle tracking velocimetry. In Proceedings ISSW, 397–404.

van Herwijnen A and Birkeland KW (2014) Measurements of snow slab displacement in extended column tests and comparison with propagation saw tests. *Cold Regions Science and Technology* **97**, 97–103.

van Herwijnen A and Jamieson B (2005) High-speed photography of fractures in weak snowpack layers. *Cold Regions Science and Technology* **43** (1-2), 71–82.

van Herwijnen A and Schweizer J (2011) Seismic sensor array for monitoring an avalanche start zone: design, deployment and preliminary results. *Journal of Glaciology* **57**(202), 267–276.

Wu HY and 5 others (2012) Eulerian video magnification for revealing subtle changes in the world. *ACM transactions on graphics (TOG)* **31**(4), 1–8.

https://doi.org/10.1017/aog.2023.36 Published online by Cambridge University Press